Interplay between diffraction and the Pancharatnam-Berry phase in inhomogeneously twisted anisotropic media

Chandroth P. Jisha,[1,*] Alessandro Alberucci,[2,3,†] Lorenzo Marrucci,[4,5] and Gaetano Assanto[2,3,6]
[1]*Centro de Física do Porto, Faculdade de Ciências, Universidade do Porto, PT-4169-007 Porto, Portugal*
[2]*Optics Laboratory, Tampere University of Technology, FI-33101 Tampere, Finland*
[3]*NooEL - Nonlinear Optics and OptoElectronics Lab, University "Roma Tre", IT-00146 Rome, Italy*
[4]*Dipartimento di Fisica, Università di Napoli Federico II, IT-80100 Naples, Italy*
[5]*CNR-ISASI, Institute of Applied Science and Intelligent Systems, IT-80078 Pozzuoli (NA), Italy*
[6]*CNR-ISC, Institute for Complex Systems, IT-00185 Rome, Italy*
(Received 30 August 2016; published 13 February 2017)

We discuss the propagation of an electromagnetic field in an inhomogeneously anisotropic material where the optic axis is rotated in the transverse plane but is invariant along the propagation direction. In such a configuration, the evolution of an electromagnetic wave packet is governed by the Pancharatnam-Berry phase (PBP), which is responsible for the appearance of an effective photonic potential. In a recent paper [ACS Photon. **3**, 2249 (2016)] we demonstrated that the effective potential supports transverse confinement. Here we find the profile of the quasimodes and show that the photonic potential arises from the Kapitza effect of light. The theoretical results are confirmed by numerical simulations, accounting for the medium birefringence. Finally, we analyze in detail a configuration able to support nonleaky guided modes.

DOI: 10.1103/PhysRevA.95.023823

I. INTRODUCTION

In the last few years, a great deal of attention has been devoted to investigating light propagation in inhomogeneously anisotropic materials, featuring a rotation of the optic axis but no variations in the local refractive indices. In such configuration, a phase distribution proportional to the local rotation angle of the optic axis can be superposed to the beam wavefront, leading to the so-called planar photonics [1–4]. Such space-dependent phase delay is due to a gradient in the Pancharatnam-Berry phase (PBP) [5,6], the latter being associated with a change in the beam polarization. For a closed path (same initial and final state) the PBP is provided by the solid angle subtended by the closed circuit on the Poincaré sphere [7].

Historically, the idea of modulating the phase of an electromagnetic wave via the PBP is due to Bomzon and co-workers, who used a metallic subwavelength grating (nowadays it would be called a two-dimensional metamaterial) [8,9]. This concept was then applied by Marrucci and collaborators to nematic liquid crystals (NLCs), which are natural materials where the pointwise orientation of the optic axis can be engineered by tailoring the boundary conditions via optical alignment techniques [10–12]. This full control over the local NLC director paved the way to new functionalities; for example, the conversion of spin angular momentum (polarization degree of freedom) to orbital angular momentum (spatial degree of freedom) [13,14] and the realization of polarization gratings in both amplitude [15,16] and phase [17–19]. Later on, the interest on PBP was boosted thanks to the introduction of metasurfaces and the demonstration of polarization-dependent optical devices [3,20], such as lenses [21,22], holograms [23], vortex plates in polymerizable NLCs [24], and deflectors based on the spin Hall effect [25,26]. Recently, the geometric phase has been used to tailor the beam wavefront upon reflection from a layer of chiral liquid crystals [4,27–29].

In this paper we investigate the propagation of finite-size electromagnetic wave packets in inhomogeneously anisotropic materials, subject to a pointwise rotation of the principal axes (Fig. 1) but invariant along the propagation direction z. Previously, by using geometric optics, other authors analyzed the dependence of the beam trajectory on the photon for an odd distribution of the rotation angle: the so-called optical Magnus effect or spin Hall effect [30,31]. For even rotations, the interplay between diffraction and PBP was discussed for wide beams as superpositions of plane waves in Refs. [32,33], whereas the approach we undertake hereby holds valid until longitudinal field components become relevant, i.e., for beams of size comparable to or narrower than the wavelength [34]. In a recent paper we showed that light propagates under the influence of an effective photonic potential, leading to leaky guided modes for bell-shaped distributions of the optic axis rotation [35] (Fig. 1). In this paper we provide a complete and detailed description of the theory—including a quantitative comparison with numerical simulations- first published in Ref. [35]. The paper is structured as follows: In Sec. II we briefly recall the basics of optical propagation in twisted anisotropic materials in the absence of diffraction. In Sec. III we generalize to the three-dimensional case the paraxial equations governing light propagation found in Ref. [35] to the case of long (with respect to the Rayleigh length) samples. We also sketch out the comparison with Pauli equation for quantum particles. In Sec. IV we first discuss the physical reason behind the absence of longitudinally invariant modes, and then we find the equations governing the quasimodes, including the higher-order components of the localized waves. In Sec. V we provide an extended physical explanation about the origin of the photonic potential as a Kapitza effect, i.e., a periodic modulation of the PBP versus propagation providing a z-independent effective photonic potential [36,37], by using

*cpjisha@gmail.com
†alessandro.alberucci@tut.fi

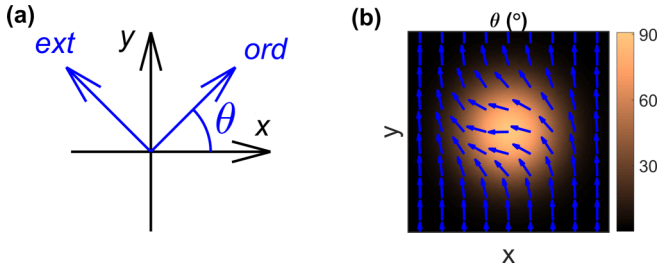

FIG. 1. (a) Definition of the rotation angle θ. (b) Gaussian distribution of the rotation angle θ on the plane xy when maximum rotation is 90°: the arrows correspond to the local optic axis (i.e., the extraordinary axis), superposed to the spatial distribution of θ represented as a color map. When $\delta = \pi$, the distribution plotted in panel (b) corresponds to a polarization-dependent lens [3,21].

the plane-wave solution shown in Sec. II. In Sec. VI the relationship between the symmetry of the twisting angle and light behavior is first recalled, and then the profile of the continuous-wave (cw) component of the quasimode is computed for the first time. In Sec. VII we check the validity of the theoretical results by using two different types of numerical simulations based on an in-house beam-propagation method (BPM) code written in the rotated reference system and on an open-access finite-difference time domain (FDTD) code. Through numerical simulations we check the validity of effective photonic potential and—in the guiding case—the accuracy of the associated quasimodes found in Sec. VI. In Sec. VIII we report the design of a nonleaky (V-shaped) waveguide in a twisted structure and test its properties via FDTD simulations. Finally, in Sec. IX we summarize the contents of this paper, pinpointing the novelties with respect to Ref. [35] and illustrating future developments, both on the theoretical and on the experimental and technological sides.

II. PANCHARATNAM-BERRY PHASE IN A THIN SAMPLE

We consider a nonmagnetic anisotropic uniaxial crystal.[1] In the reference system of the principal axes (subscript D), the relative permittivity is

$$\boldsymbol{\epsilon}_D = \begin{pmatrix} \epsilon_\perp & 0 & 0 \\ 0 & \epsilon_\parallel & 0 \\ 0 & 0 & \epsilon_\perp \end{pmatrix}, \tag{1}$$

where $\epsilon_\perp$ and $\epsilon_\parallel$ are the dielectric constants for fields oscillating normal and parallel to the optic axis $\hat{n}$, respectively. The optic axis $\hat{n}$ is normal to the wave vector $\boldsymbol{k}$ and at an angle $\theta(x,y)$ with respect to the axis y [Fig. 1(a)]. Noteworthy, $\epsilon_\perp$ and $\epsilon_\parallel$ are spatially uniform: this condition, together with the previous assumption $\hat{n} \cdot \boldsymbol{k} = 0$, rules out any refractive index changes in the transverse plane [38]. We then introduce the ordinary and extraordinary refractive indices as $n_\perp = \sqrt{\epsilon_\perp}$ and $n_\parallel = \sqrt{\epsilon_\parallel}$, respectively. The local rotation of the optic axis (i.e., of the principal axes) around z can be expressed as

$$\boldsymbol{R}(\theta) = \begin{pmatrix} \cos\theta & \sin\theta & 0 \\ -\sin\theta & \cos\theta & 0 \\ 0 & 0 & 1 \end{pmatrix}. \tag{2}$$

The matrix (2) operates on a vector in the laboratory framework xyz and yields its coordinates in the Cartesian system aligned with the local principal axes. The relative permittivity $\boldsymbol{\epsilon}$ in xyz is then provided by

$$\boldsymbol{\epsilon}(x,y) = \boldsymbol{R}[-\theta(x,y)] \cdot \boldsymbol{\epsilon}_D \cdot \boldsymbol{R}[\theta(x,y)]. \tag{3}$$

When diffraction in the anisotropic material can be neglected, light propagation can be modeled by using plane waves. In fact, the Jones formalism [39] can be employed by accounting for the transmission dependance on the transverse coordinate (x,y) through the rotation angle θ. In the plane-wave approximation, light propagation through an anisotropic slab of length z is given by

$$\begin{pmatrix} E_o(x,y,z) \\ E_e(x,y,z) \end{pmatrix} = \begin{pmatrix} e^{ik_0 n_\perp z} & 0 \\ 0 & e^{ik_0 n_\parallel z} \end{pmatrix} \cdot \begin{pmatrix} E_o(x,y,0) \\ E_e(x,y,0) \end{pmatrix}, \tag{4}$$

where E_o and E_e are the local ordinary and extraordinary polarization components, respectively [Fig. 1(a)]. Since the ordinary and extraordinary directions vary with (x,y), it is more convenient to refer to the two circularly polarized beams which are eigensolutions of the rotation operator (2). We thus introduce the circular polarization basis $\hat{L} = (\hat{x} - i\hat{y})/\sqrt{2}$ (LCP, left-circular polarization) and $\hat{R} = (\hat{x} + i\hat{y})/\sqrt{2}$ (RCP, right-circular polarization).[2] The basis transformation from linear to circular is obtained by the matrix $\boldsymbol{P}$:

$$\begin{pmatrix} E_L \\ E_R \end{pmatrix} = \boldsymbol{P} \cdot \begin{pmatrix} E_o \\ E_e \end{pmatrix} = \frac{1}{\sqrt{2}} \begin{pmatrix} 1 & -i \\ 1 & i \end{pmatrix} \cdot \begin{pmatrix} E_o \\ E_e \end{pmatrix}, \tag{5}$$

where the subscripts L and R correspond to LCP and RCP, respectively. Finally, the overall transmission of the anisotropic slab is [38]

$$\begin{pmatrix} E_L(x,y,z) \\ E_R(x,y,z) \end{pmatrix} = e^{i\bar{n}k_0 z} \begin{pmatrix} \cos\left(\frac{\delta}{2}\right) & -i\sin\left(\frac{\delta}{2}\right)e^{2i\theta} \\ -i\sin\left(\frac{\delta}{2}\right)e^{-2i\theta} & \cos\left(\frac{\delta}{2}\right) \end{pmatrix} \cdot \begin{pmatrix} E_L(x,y,0) \\ E_R(x,y,0) \end{pmatrix}, \tag{6}$$

where $\delta(z) = k_0 z \Delta n$ is the retardation between ordinary and extraordinary components, $\Delta n = n_\parallel - n_\perp$ is the birefringence, and $\bar{n} = (n_\parallel + n_\perp)/2$ is the average index of refraction [10]. Equation (6) describes a continuous exchange of power between the two circular polarizations RCP and LCP due to birefringence. Consider a purely circular polarization at the input $z = 0$ by setting, for example, $E_R(x,y,0) = 1$ and $E_L(x,y,0) = 0$. When $\delta = (2l+1)\pi$, with l an integer, the RCP wave turns into LCP: this change in polarization state is accompanied by a dynamic phase change $\Delta\phi_{\rm dyn} = (2l+1)\pi\bar{n}/\Delta n$ and a further phase shift $\Delta\phi_{\rm geo} = \pm 2\theta$ purely of geometric origin, a manifestation of the PBP [10]. Planar photonics elements based on PBP usually work in the latter regime, i.e., with the length of the anisotropic material

[1] *Mutatis mutandis*, all the following results remain valid in the more general case of a biaxial crystal.

[2] In this paper we adopt the source's point of view.

designed to achieve a π phase delay between ordinary and extraordinary components.

III. PANCHARATNAM-BERRY PHASE IN AN EXTENDED SAMPLE

Neglecting anisotropy in the diffraction operator [40], Maxwell's equations in the paraxial approximation read

$$\nabla^2\begin{pmatrix}E_x\\E_y\end{pmatrix}+k_0^2\begin{pmatrix}\epsilon_{xx}(x,y) & \epsilon_{xy}(x,y)\\ \epsilon_{yx}(x,y) & \epsilon_{yy}(x,y)\end{pmatrix}\begin{pmatrix}E_x\\E_y\end{pmatrix}=0, \quad (7)$$

where the relative permittivity is given by Eq. (3). The paraxial approximation in Eq. (7) allows one to neglect the longitudinal electric field whenever the beam size exceeds the wavelength [34].

We apply the slowly varying envelope approximation through the transformation $E_o{=}e^{ik_0 n_\perp z}\psi_o$ and $E_e{=}e^{ik_0 n_\parallel z}\psi_e$, i.e., factoring out the dynamic phase responsible for polarization rotation versus propagation. For paraxial wave packets, the second derivatives along z can be neglected and Eq. (7) yields [35]

$$\begin{aligned}2ik_0 n_\perp\frac{\partial\psi_o}{\partial z} =& -\nabla_t^2\psi_o+\left[\left(\frac{\partial\theta}{\partial x}\right)^2+\left(\frac{\partial\theta}{\partial y}\right)^2\right]\psi_o\\ &+\left(\frac{\partial^2\theta}{\partial x^2}+\frac{\partial^2\theta}{\partial y^2}\right)\psi_e e^{ik_0\Delta nz}\\ &+2\left(\frac{\partial\theta}{\partial x}\frac{\partial\psi_e}{\partial x}+\frac{\partial\theta}{\partial y}\frac{\partial\psi_e}{\partial y}\right)e^{ik_0\Delta nz}, \quad (8)\\ 2ik_0 n_\parallel\frac{\partial\psi_e}{\partial z} =& -\nabla_t^2\psi_e+\left[\left(\frac{\partial\theta}{\partial x}\right)^2+\left(\frac{\partial\theta}{\partial y}\right)^2\right]\psi_e\\ &-\left(\frac{\partial^2\theta}{\partial x^2}+\frac{\partial^2\theta}{\partial y^2}\right)\psi_o e^{-ik_0\Delta nz}\\ &-2\left(\frac{\partial\theta}{\partial x}\frac{\partial\psi_o}{\partial x}+\frac{\partial\theta}{\partial y}\frac{\partial\psi_o}{\partial y}\right)e^{-ik_0\Delta nz}, \quad (9)\end{aligned}$$

where $\nabla_t^2=\partial_x^2+\partial_y^2$. Equations (8) and (9) indicate that the waves are not subject to refractive index gradients because transverse modulation is only due to the pointwise rotation of the principal axes. For small birefringence, i.e., $n_\perp\approx n_\parallel$, Eqs. (8) and (9) resemble the Pauli equation for a charged massive particle moving in a bidimensional space [41]:

$$i\hbar\frac{\partial\boldsymbol{\psi}}{\partial t}=-\frac{\hbar^2}{2m}\nabla_{xy}^2\boldsymbol{\psi}+U(x,y)\boldsymbol{I}\cdot\boldsymbol{\psi}+\boldsymbol{H}_{LS}(x,y,t)\cdot\boldsymbol{\psi}, \quad (10)$$

with $\boldsymbol{I}$ being the identity operator and $\boldsymbol{H}_{LS}$ being the Hermitian matrix responsible for spin-orbit coupling [42];[3] $\boldsymbol{\psi}$ is a two-component spinor with elements ψ_o and ψ_e, respectively. The term containing $U(x)$ is a scalar potential acting equally on both components; the term with $\boldsymbol{H}_{LS}(x,y,t)$, which is proportional to the Pauli matrix $\boldsymbol{S}_2$, can be associated with an equivalent time-dependent magnetic field responsible for spin rotation (in our case power exchange between extraordinary and ordinary components).

[3]From the standard analogy between two-dimensional quantum mechanics and paraxial optics in the monochromatic regime, the propagation coordinate z plays the role of time.

IV. QUASIMODES IN (1 + 1) DIMENSIONS

Equations (8) and (9) do not support z-invariant modes due to the explicit dependence on the propagation coordinate z. This is due to the unavoidable power exchange between ordinary and extraordinary components when the optic axis rotates across the transverse plane. Noteworthy, the coupling between the two components does not vanish for any coordinate transformation. To clarify this, let us take a given point $P=(x_P,y_P)$ in the transverse plane with $\theta_P=\theta(P)$ and assume the wave packet to be, e.g., purely extraordinary. Due to diffraction, wavelets in P will spread towards adjacent points $P+dP$, where $\theta(P+dP)=\theta_P+d\theta$ due to the optic axis rotation. In $P+dP$, light will then be in a superposition of ordinary and extraordinary polarization states, no matter how small is the change in θ. This can also be explained through a direct analogy with the quantum mechanics of spinning particles: according to Eq. (10), photons behave like spin-$\frac{1}{2}$ particles [43] subject to a magnetic field rotating in the plane xy versus the propagation coordinate z. Thus, the commutation rule between orthogonal magnetic fields forbids the existence of stationary energy eigenstates [41]. Non-Abelian propagation of light in inhomogeneously anisotropic materials was discussed earlier in the context of geometric optics [31].

From what was stated above, no eigenmodes of Eqs. (8) or (9) exist, as confirmed by direct numerical investigations. Nonetheless, the system could support quasimodes, i.e., periodically varying solutions of finite lateral extension [44,45]. Hereafter, for the sake of simplicity we consider the one-dimensional case with $\partial_y=0$. The periodic quasimodes of Eqs. (8) and (9) can be calculated by using the ansatz

$$\psi_j=g_j(x)e^{i\sum_{p=-\infty}^{\infty}\int\overline{\beta}_p^{(j)}(x,z)dz}\quad(j=o,e), \quad (11)$$

where $g_j(x)$ are z-independent functions, whereas the complex exponentials account for spatial variations—in both phase and amplitude—on longitudinal scales equal or smaller than the beat length $\lambda/\Delta n$. The periodicity of the quasimode is ensured by setting $\overline{\beta}_p^{(j)}(x,z)=\beta_p^{(j)}(x)\exp(\frac{i2\pi p\Delta n}{\lambda}z)$ [44]. To calculate the quasimodes of a guiding PBP structure, we start from Eqs. (8) and (9) with the ansatz (11) and find

$$\begin{aligned}&-2k_0 n_\perp g_o\sum_p\overline{\beta}_p^{(o)}(x,z)\\ &=-\left\{\frac{d^2g_o}{dx^2}+2i\frac{dg_o}{dx}\frac{\partial\phi_o}{\partial x}+g_o\left[i\frac{\partial^2\phi_o}{\partial x^2}-\left(\frac{\partial\phi_o}{\partial x}\right)^2\right]\right\}\\ &+\left(\frac{d\theta}{dx}\right)^2 g_o\\ &+\left[\frac{d^2\theta}{dx^2}g_e+2\frac{d\theta}{dx}\left(\frac{dg_e}{dx}+ig_e\frac{\partial\phi_e}{\partial x}\right)\right]e^{ik_0\Delta nz}e^{i(\phi_e-\phi_o)},\end{aligned} \quad (12)$$

$$
\begin{aligned}
&- 2k_0 n_{\parallel} g_e \sum_p \overline{\beta}_p^{(e)}(x,z) \\
&= -\left\{ \frac{d^2 g_e}{dx^2} + 2i \frac{dg_e}{dx}\frac{\partial \phi_e}{\partial x} + g_e \left[i \frac{\partial^2 \phi_e}{\partial x^2} - \left(\frac{\partial \phi_e}{\partial x} \right)^2 \right] \right\} \\
&+ \left(\frac{d\theta}{dx} \right)^2 g_e \\
&- \left[\frac{d^2\theta}{dx^2} g_o + 2\frac{d\theta}{dx}\left(\frac{dg_o}{dx} + i g_o \frac{\partial \phi_o}{\partial x} \right) \right] e^{-ik_0 \Delta n z} e^{i(\phi_o - \phi_e)},
\end{aligned} \tag{13}
$$

where we introduced $\phi_j(x,z) = \sum_p \int \overline{\beta}_p^{(j)}(x,z)dz$. A quasimode defined by Eq. (11) conserves its profile in propagation provided that $\frac{d\beta_0^{(j)}}{dx} = 0$ is satisfied. Equations (12) and (13) contain periodic terms on both sides; thus each harmonic can be equalized separately. The computation is much easier if we assume that $\phi_o - \phi_e$ is constant versus z: after the derivation we verify *a posteriori* that the latter condition is satisfied to first order.

Focusing on the cw components $p = 0$, the latter satisfy the eigenvalue problem

$$
\begin{aligned}
-2\beta_0^{(o)} k_0 n_{\perp} g_o &= -\frac{d^2 g_o}{dx^2} + \left[\left(\frac{d\theta}{dx} \right)^2 \right. \\
&\left. + \frac{1}{k_0^2 (\Delta n)^2} \sum_{p=1}^{\infty} \frac{1}{p^2} \frac{d\beta_p^{(o)}}{dx} \frac{d\beta_{-p}^{(o)}}{dx} \right] g_o,
\end{aligned} \tag{14}
$$

$$
\begin{aligned}
-2\beta_0^{(e)} k_0 n_{\parallel} g_e &= -\frac{d^2 g_e}{dx^2} + \left[\left(\frac{d\theta}{dx} \right)^2 \right. \\
&\left. + \frac{1}{k_0^2 (\Delta n)^2} \sum_{p=1}^{\infty} \frac{1}{p^2} \frac{d\beta_p^{(e)}}{dx} \frac{d\beta_{-p}^{(e)}}{dx} \right] g_e.
\end{aligned} \tag{15}
$$

Thus Eqs. (14) and (15) show that the terms coupling extraordinary and ordinary waves in Eqs. (8) and (9) act on the cw components $g_j(x)$ $(j = o,e)$ as additional contributions (summations over p) to the photonic potential. Such higher-order contributions, however, from a physical point of view are expected to be relevant only when the beat length $L_B = \lambda/\Delta n$ exceeds the Rayleigh distance $L_R = \pi \overline{n} w_m^2/\lambda$, with w_m being the transverse extent of the localized mode.

When higher-order contributions can be neglected (i.e., $L_B/L_R \ll 1$), Eqs. (14) and (15) describe a wave packet evolving under the action of a photonic potential:[4]

$$
V(x) = \frac{1}{2n_j k_0} \left(\frac{d\theta}{dx} \right)^2. \tag{16}
$$

We need now to evaluate the degree of accuracy in using the potential (16) in Eqs. (14) and (15). Equations (12) and (13) also determine the profile of the functions $\beta_p^{(j)}(x)$ for $p \neq 0$, yielding the periodic evolution of the quasimode along z. The knowledge of $\beta_p^{(j)}(x)$ allows evaluating the weight of the term $\propto \sum_{p=1}^{\infty} \frac{1}{p^2} \frac{d\beta_p^{(o)}}{dx} \frac{d\beta_{-p}^{(o)}}{dx}$ on the photonic potential. For the sake of simplicity, assuming non-negligible $\beta_p^{(j)}$ only for $|p| \leqslant 1$, for $p = 1$ we get

$$
\begin{aligned}
-2k_0 n_{\perp} g_o \beta_1^{(o)} &= -\frac{\lambda}{\pi \Delta n} \frac{dg_o}{dx} \frac{d\beta_1^{(o)}}{dx} - \frac{\lambda}{2\pi \Delta n} g_o \frac{d^2 \beta_1^{(o)}}{dx^2} \\
&+ g_e \frac{d^2\theta}{dx^2} + 2\frac{dg_e}{dx}\frac{d\theta}{dx},
\end{aligned} \tag{17}
$$

$$
-2k_0 n_{\parallel} g_e \beta_1^{(e)} = -\frac{\lambda}{\pi \Delta n} \frac{dg_e}{dx} \frac{d\beta_1^{(e)}}{dx} - \frac{\lambda}{2\pi \Delta n} g_e \frac{d^2 \beta_1^{(e)}}{dx^2}. \tag{18}
$$

Similarly, for $p = -1$,

$$
-2k_0 n_{\perp} g_o \beta_{-1}^{(o)} = \frac{\lambda}{\pi \Delta n} \frac{dg_o}{dx} \frac{d\beta_{-1}^{(o)}}{dx} + \frac{\lambda}{2\pi \Delta n} g_o \frac{d^2 \beta_{-1}^{(o)}}{dx^2}, \tag{19}
$$

$$
\begin{aligned}
-2k_0 n_{\parallel} g_e \beta_{-1}^{(e)} &= \frac{\lambda}{\pi \Delta n} \frac{dg_e}{dx} \frac{d\beta_{-1}^{(e)}}{dx} + \frac{\lambda}{2\pi \Delta n} g_e \frac{d^2 \beta_{-1}^{(e)}}{dx^2} \\
&- g_o \frac{d^2\theta}{dx^2} - 2\frac{dg_o}{dx}\frac{d\theta}{dx}.
\end{aligned} \tag{20}
$$

In the general case the functions $\beta_p^{(j)}$ satisfy a second-order ordinary differential equation with coefficients given by the cw component $g_j(x)$. A drastic approximation is at hand for large Δn, when Eqs. (17)–(20) provide $\beta_1^{(e)} = \beta_{-1}^{(o)} = 0$, $\beta_1^{(o)} = -(g_e \frac{d^2\theta}{dx^2} + 2\frac{d\theta}{dx}\frac{dg_e}{dx})/(2k_0 n_{\perp} g_o)$, and $\beta_{-1}^{(e)} = (g_o \frac{d^2\theta}{dx^2} + 2\frac{d\theta}{dx}\frac{dg_o}{dx})/(2k_0 n_{\parallel} g_e)$. Substituting back into Eqs. (14) and (15), we find that the photonic potential is proportional to $(\frac{d\theta}{dx})^2 + O(\Delta n^{-2})$; as an immediate consequence, at this order of approximation [the approximation includes to set $n_{\perp} \approx n_{\parallel}$ on the LHS of Eqs. (14) and (15)] $g_o = g_e = g$. The modulation of the beam along z is now given by

$$
\beta_1^{(o)} = -\frac{\frac{d^2\theta}{dx^2} + 2\frac{d\theta}{dx}\frac{d\ln g}{dx}}{2k_0 n_{\perp}} \tag{21}
$$

and

$$
\beta_{-1}^{(e)} = \frac{\frac{d^2\theta}{dx^2} + 2\frac{d\theta}{dx}\frac{d\ln g}{dx}}{2k_0 n_{\parallel}}, \tag{22}
$$

i.e., the quasimode undergoes periodic modulation of both amplitude and phase profiles. Since $\beta_{-1}^{(e)} \approx -\beta_1^{(o)}$, $\phi_o - \phi_e$ is constant in a first approximation, in agreement with the initial hypothesis. According to Eq. (22) it is $\beta_{-1}^{(e)} \propto (w_m^2 k_0)^{-1}$, in turn providing

$$
\frac{1}{k_0^2 (\Delta n)^2} \sum_{p=1}^{\infty} \frac{1}{p^2} \frac{d\beta_p^{(e)}}{dx} \frac{d\beta_{-p}^{(e)}}{dx} \propto \left(\frac{L_B}{L_R} \right)^2;
$$

the latter result confirms that the ratio between the beating length and the Rayleigh length is the smallness parameter in our approximated treatment.

V. ORIGIN OF EFFECTIVE PHOTONIC POTENTIAL

Since we factored out the dynamic phase when introducing the fields ψ_o and ψ_e, we can speculate that the photonic

[4]Given the standard paraxial equation $2ik_0 \overline{n} \frac{\partial A}{\partial z} + \frac{\partial^2 A}{\partial x^2} + k_0^2 \Delta n^2 A = 0$, the photonic potential is defined as $V = -k_0 \frac{\Delta n^2}{2\overline{n}}$.

potential stems from the geometric phase. To prove this, in analogy with standard graded-index guides and splitting operators in numerical analysis, let us separate Eq. (7) in two portions, one accounting for diffractive spreading (second derivative along x) and one for the inhomogeneous dielectric tensor, respectively. We guess that the transverse phase distribution from the second part is able to compensate diffraction after averaging along one beat length $\lambda/\Delta n$. Owing to the absence of diffraction, the solutions of the second part of Eq. (7) correspond to Eqs. (6), i.e., the exact solutions in the plane-wave limit. On the one hand, according to Eqs. (6), when a purely circular polarization (either LCP or RCP) is launched, the dynamic phase accumulated in propagation is $k_0\overline{n}z$. This contribution is clearly constant in the transverse plane and thus cannot be responsible for the appearance of an x-dependent photonic potential. On the other hand, the terms between square brackets in Eqs. (6) provide a phase delay of geometric origin (i.e., due to variations in light polarization), which we will analyze hereafter. We adopt Pancharatnam's original approach [46,47] to calculate the phase difference $\Delta\phi_{\rm geo}$ between two different polarizations as $\Delta\phi_{\rm geo} = \arg[\boldsymbol{E}(\theta_1,z)\cdot\boldsymbol{E}^*(\theta_2,z)]$ (the superscript $*$ indicates the complex conjugate). For a purely RCP wave in $z=0$, Eqs. (6) provide

$$\Delta\phi_{\rm geo} = \arg\left[\cos^2\left(\frac{\delta}{2}\right) + \sin^2\left(\frac{\delta}{2}\right)e^{2i(\theta_2-\theta_1)}\right]. \tag{23}$$

Figure 2 graphs the geometric phase difference (23) versus δ in the plane-wave limit: $\Delta\phi_{\rm geo}$ is periodic with $\lambda/\Delta n$ and oscillates between the two extrema 0 and $2(\theta_2-\theta_1)$. The oscillation shape versus propagation z depends strongly on its amplitude: it is sinusoidal for small amplitudes (the exponential can be Taylor expanded, retaining only the linear term), whereas it is flat topped when $\theta_2-\theta_1 = 90°$; for intermediate values of $\theta_2-\theta_1$ there is a gradual transition between these two limits. Figure 2 (red dashed lines) plots the sinusoidal approximation of Eq. (23) to illustrate the discrepancy with the exact form for various relative rotations $\theta_2-\theta_1$.

Equation (23) is the key to understanding the evolution of a finite-size beam: the beam wavefront acquires a continuous geometric phase delay $\Delta\phi_{\rm geo}$, which is periodic with propagation z. Conversely, the amplitude of these phase-oscillations depends on the optic axis rotation between neighboring points in the transverse plane, i.e., on the θ distribution and its derivatives across x. Through the Kapitza effect of light, a periodic index modulation of the form $\Delta n^2 = n^2(x) - \overline{n}^2 = f(z)W(x)$ with $f(z) = \sum_l f_l \exp(2i\pi lz/\Lambda)$ yields a z-independent effective photonic potential [37]

$$V_{\rm Kap} = -k_0\frac{n^2(x)-\overline{n}^2}{2\overline{n}} = \frac{k_0\Lambda^2}{32\overline{n}\pi^2}\left(\sum_{l=-\infty}^{\infty}\frac{f_l f_{-l}}{l^2}\right)\left(\frac{dW}{dx}\right)^2. \tag{24}$$

In essence, $V_{\rm Kap}$ accounts for fast scale modulations on the continuous-wave (cw) component: the rapid oscillations in phase distribution entail a modulation of the transverse momentum k_x, the latter providing a net cumulative phase across the wavefront due to the effective kinetic energy $k_x^2/(2k_0n_j)$ [36,37].

To further support the interpretation above, we recall that the PBP is nontransitive [7]: at any given z, the phase difference between two points x_1 and x_2 with rotation equal $\theta_1=\theta(x_1)$ and $\theta_2=\theta(x_2)$, respectively, depends on the polarization state of the beam in the whole interval $[x_1\ x_2]$ or, otherwise stated, on its path on the Poincaré sphere. This is in sharp contrast with the standard dynamic phase, where the phase difference depends exclusively on initial and final states. Thus, the accumulated phase difference needs to be computed by taking adjacent points in space. Figure 2 shows that the profile (i.e., the Fourier coefficients f_l) of the periodic function $\Delta\phi_{\rm geo}$ along z [given by Eq. (23)] markedly depends on the relative rotation $\theta=\theta_2-\theta_1$, providing distinct Kapitza potentials $V_{\rm Kap}$. In the limit $|x_2-x_1|\to 0$ and infinitesimally small increments of θ, Eq. (23) gives $f(z)=\sin(\frac{2\pi\Delta nz}{\lambda})$ and $W(x)=2\overline{n}\Delta n\theta(x)$. Such an approach provides an effective z-invariant potential $V=\frac{1}{4\overline{n}k_0}(\frac{d\theta}{dx})^2$, the correct transverse profile but a factor of two smaller than Eq. (16). Discrepancy arises from the fact that the Kapitza model, elaborated in Ref. [37] for the scalar case, does not account for the complete spin-orbit interaction occurring in this case [48].

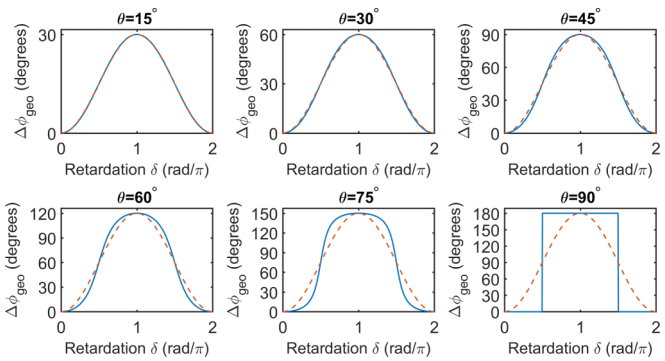

FIG. 2. Pancharatnam-Berry phase difference $\Delta\phi_{\rm geo}$ versus retardation δ between two regions differing only by a relative rotation θ when spatial dispersion is neglected, i.e., in the plane-wave limit. The blue solid lines are the exact results computed from Eq. (23); the red dashed lines are a sinusoidal approximation for $\Delta\phi_{\rm geo}$ sharing the same peak 2θ of the exact solutions.

VI. FOCUSING AND DEFOCUSING POTENTIALS

According to Eq. (16), the shape of the effective photonic potential strongly depends on the symmetry of $\theta(x)$. When θ is bell shaped [solid blue line in Fig. 3(a)], the potential is M like [dashed green line in Fig. 3(a)] and supports leaky modes [37]. Such modes can be computed with good accuracy by clipping off the edges of the potential, i.e., approximating the M well with a V profile [49]. For a Gaussian distribution of θ,

$$\theta(x) = \theta_0 e^{-\frac{x^2}{w_\theta^2}}, \tag{25}$$

Fig. 3(a) plots the associated potential

$$V = \frac{1}{2n_jk_0}\left[\frac{2x\theta_0}{w_\theta^2}\exp\left(-\frac{x^2}{w_\theta^2}\right)\right]^2.$$

Figure 4(a) graphs the resulting quasimodes versus the maximum rotation θ_0. The quasimodes computed from Eq. (16) hold valid when the higher-order contributions, i.e., the sum over p in Eqs. (14) and (15), are negligible; that is, for large-enough

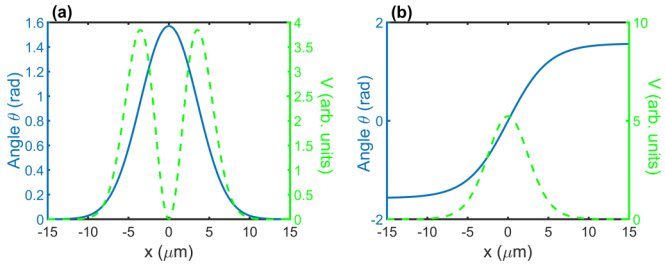

FIG. 3. (a) Rotation angle θ (blue solid line) and corresponding photonic potential (dashed green line) versus x for a Gaussian-shaped rotation of principal axes. Here $\theta_0 = \pi/2$ and $w_\theta = 5$ μm. (b) As in panel (a) but when θ has a hyperbolic tangent distribution. Here $L_\theta = 5$ μm. When $\delta = \pi$, panels (a) and (b) behave like a polarization-dependent lens and deflector, respectively.

birefringence. In Sec. VII A, BPM simulations are used to check the behavior versus the birefringence Δn. On the other hand, these results are valid as long as the mode remains confined within the central lobe of the potential [see solid and dashed lines in Fig. 4(b)], regardless of the birefringence Δn [37].

When $\theta(x)$ is odd symmetric [solid blue line in Fig. 3(b)], the photonic potential is maximum in the center (around $x = 0$) and minimum at the edges: light gets repelled from the region around $x = 0$ and no lateral confinement occurs. For example, if θ is given by

$$\theta(x) = \theta_0 \tanh\left(\frac{x}{L_\theta}\right), \tag{26}$$

the effective potential is

$$V = \frac{1}{2n_j k_0}\left\{\frac{\theta_0}{L_\theta}\left[1 - \tanh^2\left(\frac{x}{L_\theta}\right)\right]\right\}^2$$

[see the dashed green line in Fig. 3(b)].

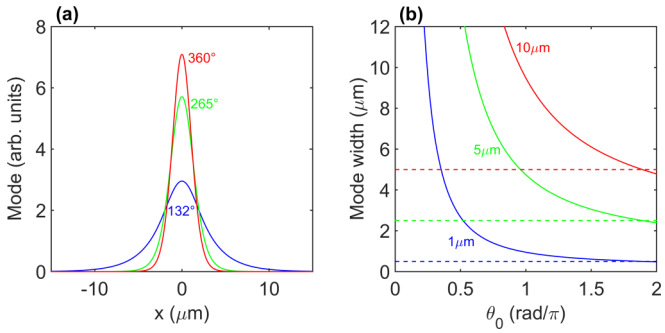

FIG. 4. (a) Intensity profile for a Gaussian distribution of θ and $w_\theta = 5$ μm; each curve is labeled with the corresponding maximum rotation θ_0. (b) Corresponding width of the quasimode versus maximum rotation angle θ_0 for three different w_θ, as labeled (solid lines). The dashed lines graph the half width of the angular distribution: above them the model is not accurate due to a finite overlap of the mode with the edges of the photonic potential [37]. Here we solved Eqs. (14) and (15) by considering only the term given by Eq. (16) when computing the quasimode; we assumed $n_\perp = 1.5$ and $n_\parallel = 1.7$.

VII. NUMERICAL SIMULATIONS

In this section we validate the theory developed above by means of numerical simulations. First, we use BPM simulations to verify that the photonic potential (16) describes accurately light propagation in a twisted anisotropic medium. Then, we use FDTD simulations to assess the paraxial approximation invoked in going from Eq. (7) to Eqs. (8) and (9). With FDTD simulations we finally address the accuracy of Eq. (7) in lieu of the exact Maxwell's equations.

A. Beam-propagation method simulations

The presence of the effective potential given by Eq. (16) can be tested by simulating Eqs. (8) and (9), which are valid in the paraxial limit. To simulate light evolution in the rotated reference system, we use a BPM code based on operator splitting and the Crank–Nicolson algorithm for diffraction.

First, we check that twisted anisotropic materials exhibit a quasi-isotropic response for propagation lengths much longer than the Rayleigh distance and large-enough birefringence. The results are shown in Fig. 5 for even [Eq. (25) and Fig. 3(a)] and odd symmetry potentials [Eq. (26) and Fig. 3(b)], with $n_\perp = 1.5$ and $\Delta n = 0.2$, a birefringence large enough to ensure that Eq. (16) is a good approximation to the exact photonic potential. For $\delta = \pi$, the even and odd distributions correspond to a polarization-dependent lens [21] and a polarization-dependent deflector based on the spin Hall effect [25], respectively. As predicted by our theory, in both cases the electromagnetic propagation is nearly independent of the input polarization. If the θ distribution is bell-shaped, diffractive spreading is counteracted and light is laterally trapped, i.e., waveguiding takes place. If θ is odd, light is repelled from the symmetry axis $x = 0$. Summarizing, Fig. 5 confirms qualitatively that light is subject to an effective potential given by Eq. (16).

Figure 6 displays light propagation for a Gaussian distribution of θ [see Eq. (25) and Fig. 3(a)] versus the maximum rotation θ_0, with $n_\perp = 1.5$ and $\Delta n = 0.2$. In agreement with

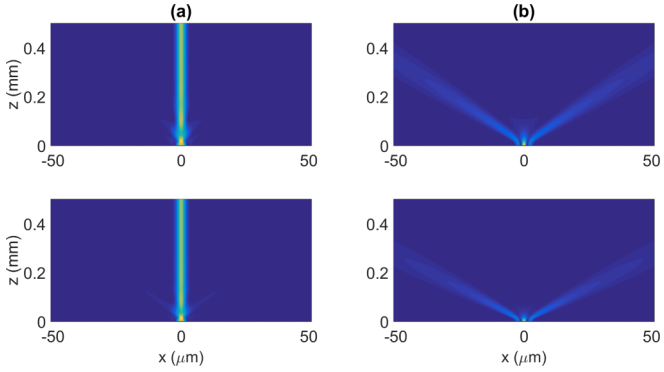

FIG. 5. Light propagation in the presence of (a) a focusing or (b) a defocusing effective potential. The first and second rows correspond to input wave packets polarized along y and x, respectively. In panel (a) and (b) the transverse distribution of θ is given by Eqs. (25) and (26), respectively. Here $\theta_0 = 360°$, $w_\theta = L_\theta = 5$ μm, $n_\perp = 1.5$, and $n_\parallel = 1.7$, the wavelength is 1064 nm. The input is a Gaussian beam of width 3 μm and with a flat phase front.

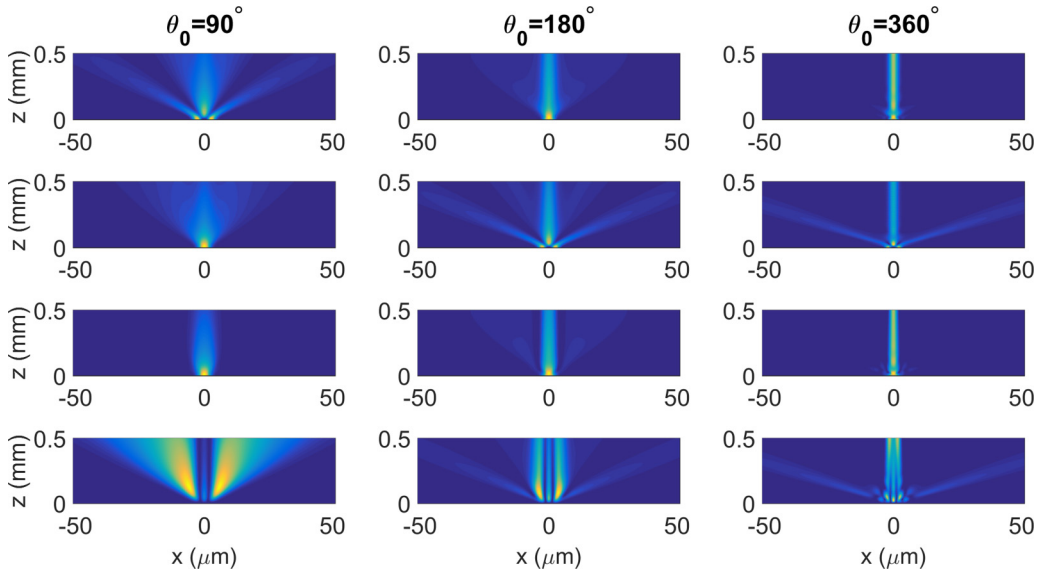

FIG. 6. Intensity distribution in the plane xz versus maximum rotation angle θ_0, computed with BPM simulations when θ is Gaussian with $w_\theta = 5$ μm, see Eq. (25); here the refractive indices are $n_\perp = 1.5$ and $n_\parallel = 1.7$ and a y-polarized Gaussian beam of waist 3 μm is launched at the input. In the first and second rows $|\psi_e|^2$ and $|\psi_o|^2$ are plotted, respectively. In the third and fourth rows the corresponding fields $|E_y|^2$ and $|E_x|^2$ are graphed in the laboratory coordinate system, respectively.

Eq. (16), as θ_0 increases the beams undergo a stronger transverse confinement due to the M-shaped potential. At the same time, the figure shows how a purely y-polarized input beam couples a fraction of its power into the x polarization owing to the pointwise rotation of the optic axis. Regardless of θ_0, strong coupling to radiation is observed due to the small spatial overlap between a linearly polarized Gaussian beam and the leaky modes.

Next, we check that our analytical model is in quantitative agreement with the actual solutions as well. It is also important to study how electromagnetic propagation depends on the birefringence Δn. To that extent, at the input we injected the quasimodes computed from the eigenvalue problem, Eqs. (12) and (13), in the limit of a large birefringence Δn, i.e., when only the action of the photonic potential provided by Eq. (16) is considered; see Fig. 4. By means of Eqs. (21) and (22), our theory predicts that the second term between square brackets in Eqs. (12) and (13) goes as $(\Delta n)^{-2}$, and thus can be neglected for large-enough birefringence. Figure 7 illustrates the quasimode evolution in the medium for $n_\perp = 1.5$ and varying the birefringence. For $\Delta n > 0.1$, guiding is clearly observed for both ψ_o and ψ_e: this implies that, for $\Delta n > 0.1$, higher-order terms in Eqs. (12) and (13) can be neglected. For larger birefringence the generation of lateral wings is observed. In this limit the difference between $n_\perp$ and $n_\parallel$ is large enough to be appreciable even on the left-hand sides of Eqs. (12) and (13), yielding a slightly anisotropic response on long scales (with respect to the beat length $\lambda/\Delta n$). For birefringence <0.1, higher-order terms in Eqs. (12) and (13) are relevant and the differences between the exact photonic potential and its approximation given by Eq. (16) cannot be neglected anymore: as a net result, guidance is lost and a polarization-dependent behavior arises. In particular, the beam remains partially trapped for birefringence down to $\Delta n \approx 0.03$ and $\Delta n \approx 0.01$ for ordinary and extraordinary inputs, respectively. Finally, the power coupled to guided modes strongly depends on the overlap between the input and the quasimode, as shown by a direct comparison between Figs. 7 and 6. We note that the overlap does not depend solely on the spatial distribution of the optical wave packet but also on its local polarization: in other words, the quasimodes are structured light.

B. Finite-difference time-domain simulations

We now check the previous results by FDTD simulations, solving directly Maxwell's equations in the time domain and without the paraxial approximation. We used the open-source code MEEP [50], taking a continuous-wave excitation at the vacuum wavelength $\lambda = 1$ μm, although our findings are valid regardless of the frequency. The source was a Gaussian-shaped collection of dipoles, of width 3 μm across x, infinitesimally narrow along z, and centered at $x = z = 0$. The emitted radiation from the source was uniformly linearly polarized. The inhomogeneous uniaxial medium started in $z = 2$ μm.

We first verify that the bell-shaped and odd θ distributions correspond to a trapping and a repulsive dynamics, respectively. We will use $n_\perp = 1.5$ and $n_\parallel = 1.7$ (thus $\Delta n = 0.2$) until otherwise specified. Figure 8(a) illustrates the wave packet evolution when the rotation angle is given by Eq. (26) [see Fig. 3(b)]: light is expelled from the central region. Figure 8(b) graphs the confining case corresponding to Eq. (25) [see Fig. 3(a)]. In both cases, the FDTD results are in excellent agreement with the BPM simulations in Fig. 5. We then concentrate on the trend of the guiding effect [θ satisfying Eq. (25)] versus the maximum rotation angle θ_0; see Fig. 9. The confinement is strongly enhanced as the maximum rotation increases, reaching a good degree of confinement for $\theta_0 = 360°$. A comparison with Fig. 6 is in excellent agreement with the BPM results.

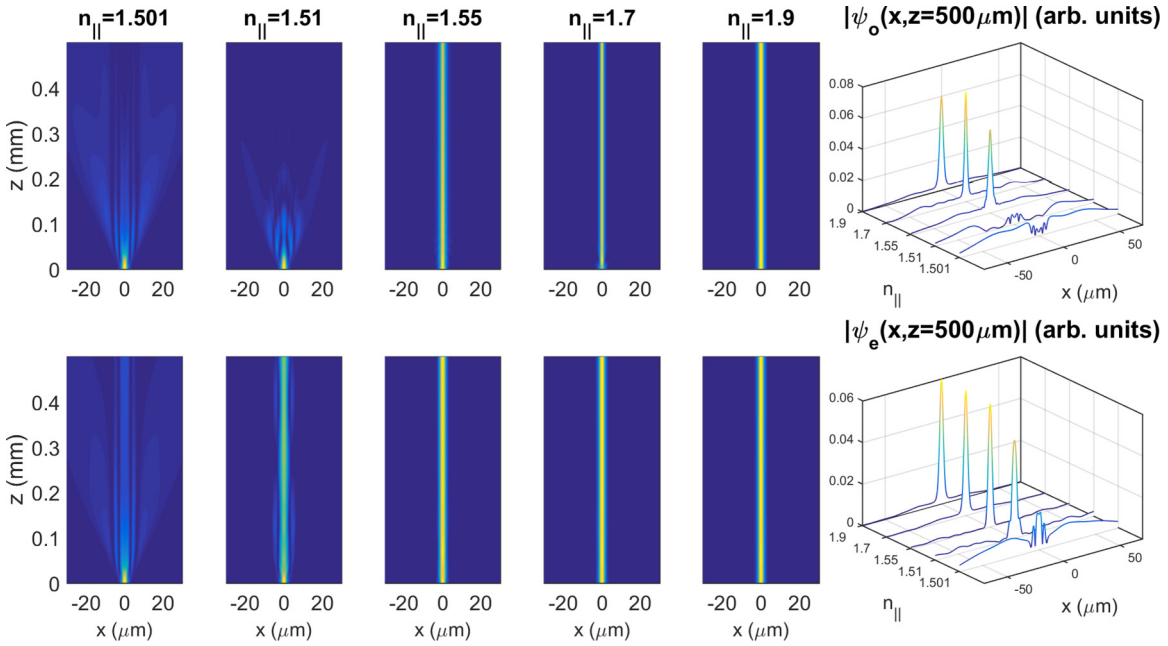

FIG. 7. Columns 1 to 5: Intensity evolution in the plane xz when the mode plotted in Fig. 4 is launched at the input $z = 0$, for different values of $n_\parallel$ as labeled (the corresponding birefringence Δn is 0.001, 0.01, 0.05, 0.2, and 0.4, from left to right, respectively). Top and bottom rows correspond to local ordinary and extraordinary polarizations, respectively. Column 6: modulus of the field $z = 500$ μm versus x and the refractive index $n_\parallel$. Here θ is Gaussian with $\theta_0 = 360^\circ$ and $w_\theta = 5$ μm, $n_\perp = 1.5$.

Quantitative details on the evolution of the input wave packet are gathered by computing its width

$$w_\eta = 2\sqrt{\int_{-L}^{L} x^2 \Pi_\eta(x)dx} \quad (\eta = I, E_j)$$

versus propagation z, with $\Pi_I = I/\int I dx$ and $\Pi_{E_j} = |E_j|^2/\int |E_j|^2 dx$ $(j = o,e)$ the probability densities for intensity and electric fields, respectively. The integrals are limited to the domain $[-L, L]$ in order to get rid of the diffracting components generated at the input interface and then radiated out. Such densities allow us to evaluate how power shares between the two orthogonal polarizations. The second row in Fig. 10 shows beam size versus z and versus the maximum rotation θ_0, respectively. The beam width w_I initially broadens due to the strong radiation emitted at the input interface and the coupling into the guide. Over longer propagation distances,

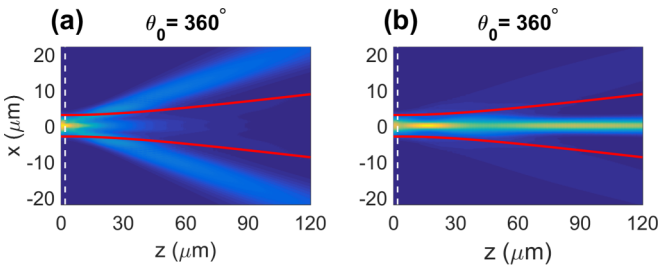

FIG. 8. FDTD simulations of the intensity distribution for (a) defocusing [θ obeying Eq. (25)] and (b) focusing [θ distributions as provided by Eq. (26)] effective potential. The input beam is linearly polarized along y, $n_\parallel = 1.7$, $w_\theta = L_\theta = 5$ μm, and $\theta_0 = 360^\circ$. The white dashed line indicates the input interface, the red solid lines show beam diffraction for $\theta_0 = 0^\circ$.

the wave packet narrows down and stabilizes to a width corresponding to the leaky mode provided by Eq. (16). We stress that, after the radiation excited at the input interface fades out, another kind of coupling to radiation occurs, inherent to leaky modes in M-shaped waveguides [49]. The corresponding losses strongly depend on θ_0, becoming negligible after several Rayleigh distances for modes narrower than the guiding core of the M guide. The two different contributions to radiation can be discriminated more easily by BPM simulations, because in that case the input can be tailored to match the effective mode. The role of the overlap in $z = 0$ can be evaluated by comparing Figs. 6 and 7 for $n_\parallel = 1.7$ (corresponding to $\Delta n = 0.2$) and $\theta_0 = 360^\circ$: when a Gaussian beam is launched, at the input interface two additional beams are emitted, tilted to left and right of the impinging wave vector by the same angle. These side lobes are strongly dampened when the quasimode is launched. The radiation loss in the bulk, related with the leaky nature of the quasimode, can be better appreciated for $\theta_0 = 180^\circ$ and $n_\parallel = 1.7$. In fact, once radiation from the interface has moved away from the central region, the amplitude of the central lobe slightly decreases with z, both in BPM (Fig. 6) and in FDTD simulations (Fig. 9).

We finally investigate light propagation versus input polarization and birefringence; the results are shown in Fig. 11. For $\Delta n > 0.2$, the propagation is almost independent from the input polarization; at lower birefringence, the propagation is polarization dependent. These findings match the BPM results, see e.g., Fig. 7. When $n_\parallel = 1.501$ and $n_\parallel = 1.51$ (corresponding to $\Delta n = 0.001$ and $\Delta n = 0.01$, respectively), light propagation is polarization-dependent both in BPM and FDTD simulations, owing to the action of the higher-order contributions, the latter modifying the shape of the photonic potential with respect to the approximated formula (16). In

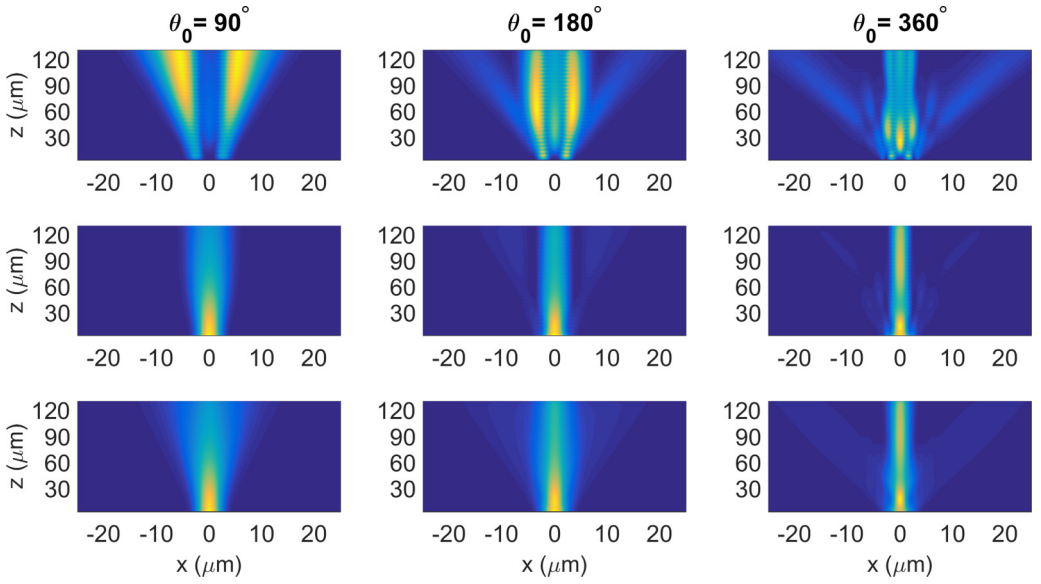

FIG. 9. FDTD simulations versus θ_0. Evolution of $|E_x|^2$ (first row), $|E_y|^2$ (second row) and the overall intensity $|E_x|^2 + |E_y|^2$ (third row) in the plane xz. The input beam is linearly polarized along y.

both cases, light trapping is stronger for input beams polarized along y than along x. Specifically, for $n_\parallel = 1.51$, input wave packets polarized along y are confined while the orthogonal polarization spreads out, whereas for $n_\parallel = 1.501$ wave packet widens irrespectively of the input polarization. Noteworthy, when BPM (Fig. 7) and FDTD (Fig. 11) are compared, it is important to recall that propagation lengths in the former are much larger than in the latter.

VIII. NONLEAKY WAVEGUIDES

Equation (16) allows tailoring the profile $\theta(x)$ of the continuous rotation to yield a bell-shaped effective well able to support nonleaky guided modes. Since the lowest value of the potential is zero, for a nonleaky electromagnetic waveguide the derivative $d\theta/dx$ must vanish in $x = 0$, corresponding to a local extremum of θ. Therefore, $\theta(x)$ needs to be an even function. The condition $V(x) > 0$ for $|x| \to \infty$ must be satisfied to get evanescent waves beyond the waveguide edges. Moreover, a realistic waveguide must be (transversely) finite; hence, we have to impose a linear trend $\theta(x) = \alpha(|x| - x^{\diamond})$ for $|x| > x_0$, with x_0 linked to the width of the guide. Finally, for $|x| < x_0$ we need to select a convex even function θ so that the potential (16) has a relative minimum in $x = 0$. The

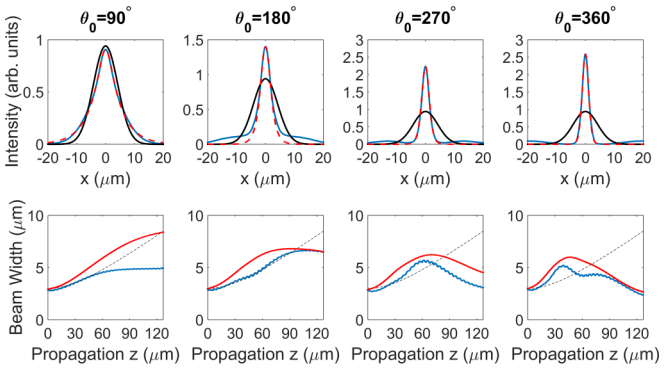

FIG. 10. Direct comparison between analytic theory and FDTD simulations when the input is linearly polarized along y, θ has is Gaussian and $w_\theta = 5$ μm. Upper panels: overall intensity cross-sections calculated at $z = 120$ μm for a Gaussian wave packet undergoing diffraction when $\theta_0 = 0°$ (solid black lines) and the dielectric tensor is transversely rotated (solid blue lines). The red dashed lines are the corresponding quasimodes from Eqs. (14) and (15). Lower panels: wave packet width versus propagation distance z using Π_{E_y} (blue solid line) and Π_I (red solid lines) for the probability densities. The black dashed line corresponds to a diffracting Gaussian beam in the limit $\theta_0 = 0°$. Here $L = 10$ μm.

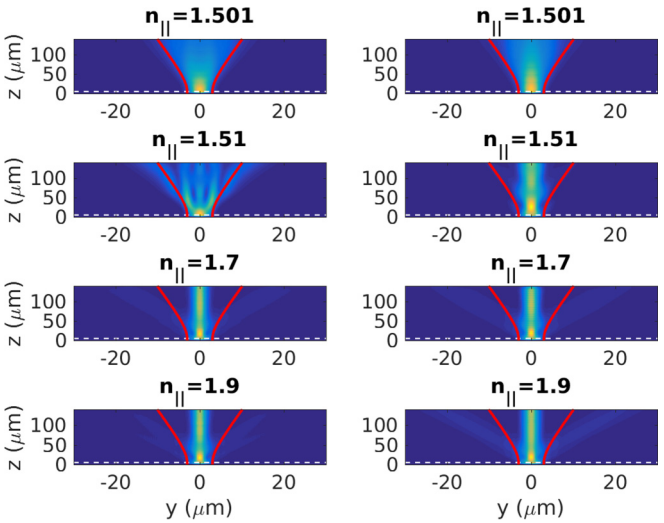

FIG. 11. FDTD simulations versus birefringence for a fixed θ profile. The beam is linearly polarized along x (left column) and y (right column). Birefringence Δn is 0.001, 0.01, 0.2, and 0.4, from the top to bottom row, respectively. The red solid lines show the diffracting case, the dashed white lines correspond to the initial section of the anisotropic medium. Here $n_\perp = 1.5$, $\theta_0 = 360°$, and $w_\theta = 5$ μm.

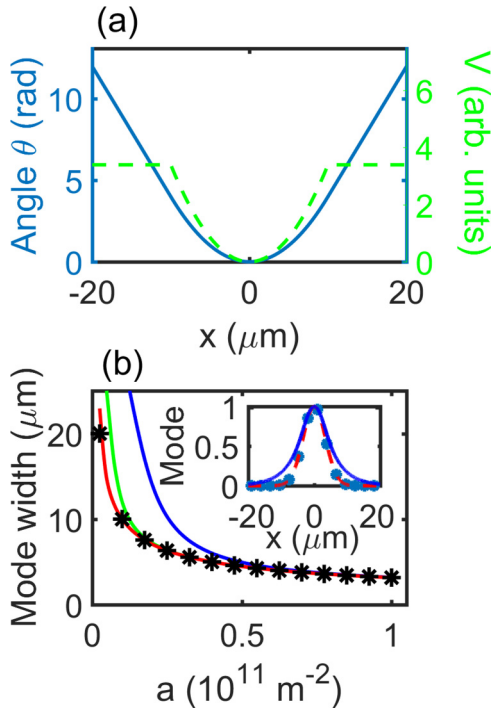

FIG. 12. V-shaped PBP waveguide. (a) Rotation angle θ (blue solid line) and corresponding potential V from Eq. (27) (green dashed line) for $x_0 = 10$ μm and $a = 4\times10^{10}$ m^{-2}. (b) Mode width versus a for (top to bottom curves) $x_0 = 5$ μm (blue line), 10 μm (green), and 20 μm (red). The stars graph the width w_G of the Gaussian fundamental mode of the parabolic potential in the limit $x_0 \to \infty$. Inset: mode intensity profile when $a = 2\times10^{10}$ m^{-2} for $x_0 = 5$ μm (blue solid line) and $x_0 = 20$ μm (red dashed line). Blue stars represent the Gaussian mode when $x_0 \to \infty$.

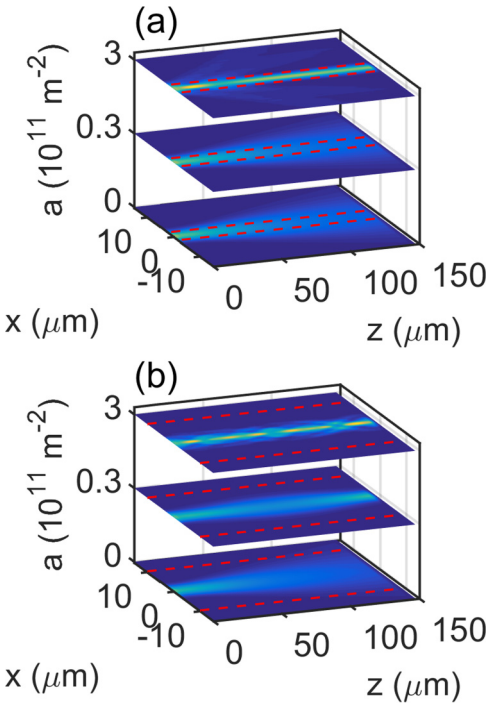

FIG. 13. V-shaped PBP waveguide. FDTD simulations in the plane xz for $a = 0$, 3×10^{10}, and 3×10^{11}m^{-2}, respectively (slices from bottom to top) when (a) $x_0 = 2$ μm and (b) $x_0 = 10$ μm. The red dashed lines correspond to the straight lines $x = \pm|x_0|$, i.e., the waveguide edges.

simplest choice is a parabolic profile of the form ax^2, such that the resulting photonic potential V is

$$V(x) = \begin{cases} \frac{2a^2x^2}{n_j k_0} & \text{for } |x| \leqslant x_0 \\ \frac{2a^2x_0^2}{n_j k_0} & \text{for } |x| > x_0, \end{cases} \tag{27}$$

where we satisfied the continuity conditions on $\theta(x)$ and $d\theta/dx$ by setting $x^{\diamond} = x_0/2$ and $\alpha = 2ax_0$, respectively. An example is graphed in Fig. 12(a).

In the limit $x_0 \to \infty$ the photonic potential is purely parabolic, thus supporting an infinite number of guided modes, the fundamental one being Gaussian with field proportional to e^{-x^2/w_G^2} and width $w_G = 1/\sqrt{a}$. The fundamental mode of the PBP waveguide defined by Eq. (27) corresponds to such a solution for widths w_G much smaller than x_0, as confirmed in Fig. 12(b) graphing the exact modes of the potential Eq. (27). We analyze the beam propagation in such PBP waveguide by means of FDTD simulations: a synopsis of the results is available in Figs. 13(a) and 13(b). As the coefficient a increases starting from zero, the wave packet undergoes transverse confinement. In agreement with Fig. 12(b), narrower waveguides (i.e., smaller x_0) yield lower field confinement.

IX. CONCLUSIONS AND PERSPECTIVES

In this paper we examined the propagation of electromagnetic waves in inhomogeneously anisotropic media, locally twisted in the transverse plane but invariant in propagation. First, we expanded the results reported in Ref. [35], providing a deeper insight of the physical principles and extending the theoretical computations. As a matter of fact, we showed that light propagates under the influence of an effective photonic potential due to the spin-orbit interaction, which originates from the periodic modulation of the Pancharatnam-Berry phase versus propagation via the Kapitza effect. Noteworthy, this photonic potential features a quasi-isotropic behavior, despite the locally anisotropic response of the material. The attracting or repelling character of the potential strictly depends on the symmetry of the optic axis rotation: in particular, guiding structures correspond to bell-shaped distributions. Due to the inherent power exchange between the ordinary and the extraordinary components, the system does not support z-invariant modes [30] but quasiperiodic modes, in agreement with the Floquet theorem. While in general the guided modes are leaky owing to an M-shaped potential, we designed a distribution yielding a V-shaped potential and truly guided modes.

With respect to Ref. [35], all of these results have been (qualitatively and quantitatively) validated by means of BPM and FDTD numerical simulations. In particular, here we used a BPM written in the rotated framework, specifically developed for this problem. We also demonstrated a very good agreement between BPM and FDTD: this is a very important result given

that BPM codes are much less demanding than FDTD from the computational point of view. Our BPM code will be thus relevant for the numerical analysis of q plates and similar devices, nowadays mainly described by means of simple plane-wave models. Both the numerical techniques confirmed that our theory provides a very good approximation of the confined mode for a vast range of parameters. With respect to the latter statement, we also explored the limits of our analytical model versus the medium birefringence and maximum rotation angle, both for weakly and highly anisotropic materials.

Our findings pave the way to the design and realization of a new kind of electromagnetic waveguides, with the presented mechanism valid regardless of frequency. Twisted structures can be realized, for example, by using liquid crystals [4,10,51], laser-written anisotropic glasses [26], and metamaterials [3,5,52]. With respect to Ref. [38], the geometry proposed herein is much simpler to realize because it is structured only in the transverse plane. Furthermore, the longitudinal homogeneity of the sample inhibits back reflections, an important detrimental effect when fabricating high-quality waveguides. Our results can be generalized to more complicated and exotic anisotropic responses, including, e.g., magneto-electric coupling [53–59]. Several future developments can be envisaged, including the systematic investigation of light trapping versus geometrical and material parameters of the structure, and the usage of our model to find the periodic components of the quasimode. It will be also interesting to investigate the interplay between the Rytov-Vladimirskii-Berry and the Pancharatnam-Berry phases which are both of geometric origin [42], and the connection of our system with the recently introduced gauge optics [60,61].

From a more fundamental point of view, this works is an important contribution to the analogy between light propagation in anisotropic materials and propagation of spin-$\frac{1}{2}$ particles in magnetic fields: in fact, confinement based on geometric phase can be readily transposed to matter waves, e.g., charged particles in a Paul trap [62].

ACKNOWLEDGMENTS

C.P.J. gratefully acknowledges Fundação para a Ciência e a Tecnologia, POPH-QREN, and FSE (FCT, Portugal) for the fellowship SFRH/BPD/77524/2011; she also thanks the Optics Laboratory in Tampere for their hospitality. A.A. and G.A. thank the Academy of Finland through the Finland Distinguished Professor Grant No. 282858. L.M. acknowledges support from the European Research Council (ERC), under Grant No. 694683, PHOSPhOR.

[1] A. V. Kildishev, A. Boltasseva, and V. M. Shalaev, Planar photonics with metasurfaces, Science **339**, 1232009 (2013).
[2] N. Yu and F. Capasso, Flat optics with designer metasurfaces, Nat. Mater. **13**, 139 (2014).
[3] D. Lin, P. Fan, E. Hasman, and M. L. Brongersma, Dielectric gradient metasurface optical elements, Science **345**, 298 (2014).
[4] J. Kobashi, H. Yoshida, and M. Ozaki, Planar optics with patterned chiral liquid crystals, Nat. Photon. **10**, 389 (2016).
[5] Z. Bomzon, G. Biener, V. Kleiner, and E. Hasman, Space-variant Pancharatnam-Berry phase optical elements with computer-generated subwavelength gratings, Opt. Lett. **27**, 1141 (2002).
[6] L. Marrucci, C. Manzo, and D. Paparo, Pancharatnam-Berry phase optical elements for wavefront shaping in the visible domain: Switchable helical modes generation, Appl. Phys. Lett. **88**, 221102 (2006).
[7] M. V. Berry, The adiabatic phase and Pancharatnam's phase for polarized light, J. Mod. Opt. **34**, 1401 (1987).
[8] Z. Bomzon, V. Kleiner, and E. Hasman, Formation of radially and azimuthally polarized light using space-variant subwavelength metal stripe gratings, Appl. Phys. Lett. **79**, 1587 (2001).
[9] E. Hasman, V. Kleiner, G. Biener, and A. Niv, Polarization dependent focusing lens by use of quantized Pancharatnam-Berry phase diffractive optics, Appl. Phys. Lett. **82**, 328 (2003).
[10] L. Marrucci, C. Manzo, and D. Paparo, Optical Spin-to-Orbital Angular Momentum Conversion in Inhomogeneous Anisotropic Media, Phys. Rev. Lett. **96**, 163905 (2006).
[11] S. Slussarenko, A. Murauski, T. Du, V. Chigrinov, L. Marrucci, and E. Santamato, Tunable liquid crystal q-plates with arbitrary topological charge, Opt. Express **19**, 4085 (2011).
[12] J. Kim, Y. Li, M. N. Miskiewicz, C. Oh, M. W. Kudenov, and M. J. Escuti, Fabrication of ideal geometric-phase holograms with arbitrary wavefronts, Optica **2**, 958 (2015).
[13] T. Bauer, P. Banzer, E. Karimi, S. Orlov, A. Rubano, L. Marrucci, E. Santamato, R. W. Boyd, and G. Leuchs, Observation of optical polarization Möbius strips, Science **347**, 964 (2015).
[14] D. Naidoo, F. S. Roux, A. Dudley, I. Litvin, B. Piccirillo, L. Marrucci, and A. Forbes, Controlled generation of higher-order Poincaré sphere beams from a laser, Nat. Photon. **10**, 327 (2016).
[15] T. Todorov and L. Nikolova, Spectrophotopolarimeter: Fast simultaneous real-time measurement of light parameters, Opt. Lett. **17**, 358 (1992).
[16] F. Gori, Measuring Stokes parameters by means of a polarization grating, Opt. Lett. **24**, 584 (1999).
[17] C. Provenzano, P. Pagliusi, and G. Cipparrone, Electrically tunable two-dimensional liquid crystals gratings induced by polarization holography, Opt. Express **15**, 5872 (2007).
[18] N. V. Tabiryan, S. R. Nersisyan, T. J. White, T. J. Bunning, D. M. Steeves, and B. R. Kimball, Transparent thin film polarizing and optical control systems, AIP Adv. **1**, 022153 (2011).
[19] U. Ruiz, P. Pagliusi, C. Provenzano, and G. Cipparrone, Highly efficient generation of vector beams through polarization holograms, Appl. Phys. Lett. **102**, 161104 (2013).
[20] N. M. Litchinitser, Photonic multitasking enabled with geometric phase, Science **352**, 1177 (2016).
[21] F. S. Roux, Geometric phase lens, J. Opt. Soc. Am. A **23**, 476 (2006).
[22] M. Khorasaninejad, W. T. Chen, R. C. Devlin, J. Oh, A. Y. Zhu, and F. Capasso, Metalenses at visible wavelengths: Diffraction-limited focusing and subwavelength resolution imaging, Science **352**, 1190 (2016).
[23] G. Zheng, H. Mhlenbernd, M. Kenney, G. Li, T. Zentgraf, and S. Zhang, Metasurface holograms reaching 80% efficiency, Nat. Nanotechnol. **10**, 308 (2015).

[24] S. Nersisyan, N. Tabiryan, D. M. Steeves, and B. R. Kimball, Fabrication of liquid crystal polymer axial waveplates for UV-IR wavelengths, Opt. Express **17**, 11926 (2009).
[25] G. Li, M. Kang, S. Chen, S. Zhang, E. Yue-Bun Pun, K. W. Cheah, and J. Li, Spin-enabled plasmonic metasurfaces for manipulating orbital angular momentum of light, Nano Lett. **13**, 4148 (2013).
[26] X. Ling, X. Zhou, X. Yi, W. Shu, Y. Liu, S. Chen, H. Luo, S. Wen, and D. Fan, Giant photonic spin Hall effect in momentum space in a structured metamaterial with spatially varying birefringence, Light: Sci. Appl. **4**, e290 (2015).
[27] M. Rafayelyan, G. Tkachenko, and E. Brasselet, Reflective Spin-Orbit Geometric Phase from Chiral Anisotropic Optical media, Phys. Rev. Lett. **116**, 253902 (2016).
[28] J. Kobashi, H. Yoshida, and M. Ozaki, Polychromatic Optical Vortex Generation from Patterned Cholesteric Liquid Crystals, Phys. Rev. Lett. **116**, 253903 (2016).
[29] R. Barboza, U. Bortolozzo, M. G. Clerc, and S. Residori, Berry Phase of Light under Bragg Reflection by Chiral Liquid-Crystal Media, Phys. Rev. Lett. **117**, 053903 (2016).
[30] K. Yu. Bliokh, D. Yu. Frolov, and Yu. A. Kravtsov, Non-Abelian evolution of electromagnetic waves in a weakly anisotropic inhomogeneous medium, Phys. Rev. A **75**, 053821 (2007).
[31] K. Y. Bliokh, Y. Gorodetski, V. Kleiner, and E. Hasman, Coriolis Effect in Optics: Unified Geometric Phase and Spin Hall Effect, Phys. Rev. Lett. **101**, 030404 (2008).
[32] G. F. Calvo and A. Picón, Spin-induced angular momentum switching, Opt. Lett. **32**, 838 (2007).
[33] E. Karimi, B. Piccirillo, L. Marrucci, and E. Santamato, Light propagation in a birefringent plate with topological charge, Opt. Lett. **34**, 1225 (2009).
[34] M. Lax, W. H. Louisell, and W. B. McKnight, From Maxwell to paraxial wave optics, Phys. Rev. A **11**, 1365 (1975).
[35] A. Alberucci, C. P. Jisha, L. Marrucci, and G. Assanto, Electromagnetic confinement via spin-orbit interaction in anisotropic dielectrics, ACS Photon. **3**, 2249 (2016).
[36] P. L. Kapitza, Dynamic stability of a pendulum when its point of suspension vibrates, Sov. Phys. JETP **21**, 588 (1951).
[37] A. Alberucci, L. Marrucci, and G. Assanto, Light confinement via periodic modulation of the refractive index, New J. Phys. **15**, 083013 (2013).
[38] S. Slussarenko, A. Alberucci, C. P. Jisha, B. Piccirillo, E. Santamato, G. Assanto, and L. Marrucci, Guiding light via geometric phases, Nat. Photon. **10**, 571 (2016).
[39] R. Clark Jones, A new calculus for the treatment of optical systems I. Description and discussion of the calculus, J. Opt. Soc. Am. **31**, 488 (1941).
[40] M. Kwasny, U. A. Laudyn, F. A. Sala, A. Alberucci, M. A. Karpierz, and G. Assanto, Self-guided beams in low-birefringence nematic liquid crystals, Phys. Rev. A **86**, 013824 (2012).
[41] P. A. M. Dirac, *The Principles of Quantum Mechanics* (Oxford Science Publications, Oxford, 1999).
[42] K. Y. Bliokh, F. J. Rodríguez-Fortuno, F. Nori, and A. V. Zayats, Spin-orbit interactions of light, Nat. Photon. **9**, 796 (2015).
[43] K. E. Ballantine, J. F. Donegan, and P. R. Eastham, There are many ways to spin a photon: Half-quantization of a total optical angular momentum, Sci. Adv. **2**, e1501748 (2016).
[44] J. H. Shirley, Solution of the Schrödinger equation with a Hamiltonian periodic in time, Phys. Rev. **138**, B979 (1965).
[45] L. S. Brown, Quantum Motion in a Paul Trap, Phys. Rev. Lett. **66**, 527 (1991).
[46] S. Pancharatnam, Generalized theory of interference, and its applications, Proc. Indian Acad. Sci. A **44**, 247 (1956).
[47] M. V. Berry, Pancharatnam, virtuoso of the Poincaré sphere: An appreciation, Curr. Sci. **67**, 220 (1994).
[48] K. Y. Bliokh, C. T. Samlan, C. Prajapati, G. Puentes, N. K. Viswanathan, and F. Nori, Spin-Hall effect and circular birefringence of a uniaxial crystal plate, Optica **3**, 1039 (2016).
[49] J. Hu and C. R. Menyuk, Understanding leaky modes: Slab waveguide revisited, Adv. Opt. Photon. **1**, 58 (2009).
[50] A. F. Oskooi, D. Roundy, M. Ibanescu, P. Bermel, J. D. Joannopoulos, and S. G. Johnson, MEEP: A flexible free-software package for electromagnetic simulations by the FDTD method, Comput. Phys. Commun. **181**, 687 (2010).
[51] A. D'Alessandro, L. Martini, G. Gilardi, R. Beccherelli, and R. Asquini, Polarization-independent nematic liquid crystal waveguides for optofluidic applications, IEEE Photon. Technol. Lett. **27**, 1709 (2015).
[52] A. N. Askarpour, Y. Zhao, and A. Alù, Wave propagation in twisted metamaterials, Phys. Rev. B **90**, 054305 (2014).
[53] J. B. Pendry, A. J. Holden, D. J. Robbins, and W. J. Stewart, Magnetism from conductors and enhanced nonlinear phenomena, IEEE Trans. Microwave Theory Tech. **47**, 2075 (1999).
[54] D. R. Smith and D. Schurig, Electromagnetic Wave Propagation in Media with Indefinite Permittivity and Permeability Tensors, Phys. Rev. Lett. **90**, 077405 (2003).
[55] A. Ghosh, N. K. Sheridon, and P. Fischer, Voltage-controllable magnetic composite based on multifunctional polyethylene microparticles, Small **4**, 1956 (2008).
[56] A. B. Khanikaev, S. H. Mousavi, W.-K. Tse, M. Kargarian, A. H. MacDonald, and G. Shvets, Photonic topological insulator, Nat. Mater. **12**, 233 (2013).
[57] C. Pfeiffer and A. Grbic, Metamaterial Huygens' Surfaces: Tailoring Wave fronts with Reflectionless Sheets, Phys. Rev. Lett. **110**, 197401 (2013).
[58] K. Y. Bliokh, Y. S. Kivshar, and F. Nori, Magnetoelectric Effects in Local Light-Matter Interactions, Phys. Rev. Lett. **113**, 033601 (2014).
[59] V. S. Asadchy, Y. Ra'di, J. Vehmas, and S. A. Tretyakov, Functional Metamirrors using Bianisotropic Elements, Phys. Rev. Lett. **114**, 095503 (2015).
[60] K. Fang and S. Fan, Controlling the Flow of Light Using the Inhomogeneous Effective Gauge Field that Emerges from Dynamic Modulation, Phys. Rev. Lett. **111**, 203901 (2013).
[61] Q. Lin and S. Fan, Light Guiding by Effective Gauge Field for Photons, Phys. Rev. X **4**, 031031 (2014).
[62] W. Paul, Electromagnetic traps for charged and neutral particles, Rev. Mod. Phys. **62**, 531 (1990).